Title
Phreatic seepage flow through an earth dam with an impeding strip

Permalink
https://escholarship.org/uc/item/56z3j21b

Journal
Computational Geosciences, 24(1)

ISSN
1420-0597

Authors
Kacimov, AR
Yakimov, ND
Šimůnek, J

Publication Date
2020-02-01

DOI
10.1007/s10596-019-09879-8

Peer reviewed

ORIGINAL PAPER

Phreatic seepage flow through an earth dam with an impeding strip

A. R. Kacimov [1] (iD) · N. D. Yakimov [2] · J. Šimůnek [3]

Abstract
New mathematical models are developed and corresponding boundary value problems are analytically and numerically solved for Darcian flows in earth (rock)–filled dams, which have a vertical impermeable barrier on the downstream slope. For saturated flow, a 2-D potential model considers a free boundary problem to Laplace's equation with a traveling-wave phreatic line generated by a linear drawup of a water level in the dam reservoir. The barrier re-directs seepage from purely horizontal (a seepage face outlet) to purely vertical (a no-flow boundary). An alternative model is also used for a hydraulic approximation of a 3-D steady flow when the barrier is only a partial obstruction to seepage. The Poisson equation is solved with respect to Strack's potential, which predicts the position of the phreatic surface and hydraulic gradient in the dam body. Simulations with HYDRUS, a FEM-code for solving Richards' PDE, i.e., saturated-unsaturated flows without free boundaries, are carried out for both 2-D and 3-D regimes in rectangular and hexagonal domains. The Barenblatt and Kalashnikov closed-form analytical solutions in non-capillarity soils are compared with the HYDRUS results. Analytical and numerical solutions match well when soil capillarity is minor. The found distributions of the Darcian velocity, the pore pressure, and total hydraulic heads in the vicinity of the barrier corroborate serious concerns about a high risk to the structural stability of the dam due to seepage. The modeling results are related to a "forensic" review of the recent collapse of the spillway of the Oroville Dam, CA, USA.

✉ A. R. Kacimov
anvar@squ.edu.om; akacimov@gmail.com; https://www.squ.edu.om/agr/Academics/Departments/Soil-Water-and-Agricultural-Engineering

N. D. Yakimov
nyakimov@inbox.ru

J. Šimůnek
jsimunek@ucr.edu

[1] Department of Soils, Water and Agricultural Engineering, Sultan Qaboos University, POBox 34, Al-Khod, 123 Muscat, Sultanate of Oman

[2] Department of Thermal Engineering, Kazan State Power Engineering University, Kazan, Russia

[3] Department of Environmental Sciences, University of California at Riverside, Riverside, CA, USA

1 Introduction

Barriers and other impermeable or low-permeable entities, naturally occurring or engineered inside porous massifs, significantly alter the incident seepage flows [1]. In geotechnical engineering of earth dams, several types of barriers are designed for reducing seepage: clay cores, sheet pilings, cut-off-walls, among others. A motivating example for this paper is the Oroville Dam (California) crisis of 2017. On the eve of this crisis, Yakimov and Kacimov [2] accentuated the necessity to study a potentially dangerous phenomenon of seepage across cutoff-walls in porous foundations of dams. In this type of Darcian flow, invisible but insidious hydraulic gradients across the barrier can cause its mechanical suffusion and deterioration of counter-seepage functions. In February 2017, the main spillway of the Oroville Dam failed. Figure 1 shows a photo, where points F_1 and F_2 will be explained later, and d is half-width of the spillway chute.

The Oroville Dam proper is an engineered earthen dam that forms a reservoir known as Lake Oroville behind it. The crisis involved the need to release water from the reservoir during a period of rising water levels and significant precipitation (see [3, 4]). The initial releases were directed to the main concrete-lined spillway constructed adjacent to the dam proper along the top of a bounding geologic formation. Part one of the crisis involved the appearance of a crater in the concrete spillway during the discharge, the subsequent uplifting of a part of the concrete slab, and the exposure of the geologic materials underneath to significant erosion from high velocity flows. Part two of the crisis involved a redirection of releases to a second, unlined emergency spillway adjacent to the main spillway, across the same body of poor geologic materials, which led to additional significant erosion there. Although the cause of the erosion in both cases was triggered by the flows occurring across the top surface of this formation, its cause (in both cases) was largely attributed to an improper understanding of how the (natural) geologic materials within the formation (including, presumably, resident saturation levels) would

Fig. 1 Photo of a collapsed spillway of the Oroville dam

behave under spillway use. It is key to note that the failed geologic materials were not part of the engineered dam proper and that their intrinsic integrity under conditions of main spillway use had been previously questioned.

The event spurred a surge of debates in the media, concerns of NGOs/public, comments by academics (e.g., Bea [5–7]), and official "forensic" investigations (see e.g. [3]), which involved professional geotechnical engineers, professional societies, and federal/state authorities (i.e., US Army Corps of Engineers (USACoE), The Association of State Dam Safety Officials, U.S. Society on Dams, Canadian Dam Association, Federal Energy Regulatory Commission, California Department of Water Resources, among others). For example, Bea et al. [8], Cobos-Roa and Bea [9], and Steedman and Sharp [10], among others, reviewed the failure of the New Orleans levees and pinpointed the importance of seepage erosion. Bea [5, 6], investigating a similar failure in 2017, raised a question: did a sudden rise of the reservoir level of the Oroville dam induce seepage in the part of the dam embankment close to it spillway and were these major factors that have contributed to its collapse?

As after any catastrophe of this kind, the spotlight is on the durability of hydraulic structures, especially "old" ones. The inventory of USACoE includes almost 90,000 of dams in the USA. NRC [11] identified 74,119 earth (rock)-filled dams in the National Inventory of Dams (NID) [67] (USACoE [68]) and 22,500 km of levees in the National Levee Database; according to NRC, about 56% of dams in NID will be older than 50 years by 2020. Seepage-triggered failures of "new" dams also generate a number of studies on the internal erosion of earth-rock fillings of embankments (see, for example, [12, 13]).

Allegedly anticipated effects of global warming suggest that structures will be subjected more often to extreme hydrologic events, which are characterized by intermittent droughts and torrential rains of ever-increasing amplitudes (Vahedifard et al., [14], Vano et al. [15]). For example, Lake Oroville (behind the Oroville dam) was in the center of public attention for several years during the most recent drought in California. The dried-out banks and the bed of the lake and the embankment itself were shown in the media as an illustration of "climate change," just before the February-17 deluge.

Reservoirs like Lake Oroville are operated to achieve two, often conflicting goals: (1) storage of water for use in the dry summer months and (2) flood prevention through the maintenance of an open storage volume, which often requires controlled releases even when not needed for water supply. Thus, operationally, water levels are typically kept lower in anticipation of an upcoming rainy season. The effects of climatic swings that are now being experienced suggest that the strategy for this kind of dual-use operation must be reevaluated. These swings from very dry to flooded conditions of earthworks exacerbate the natural aging of dams, many of which

were designed decades ago for hydrologically relatively less variable regimes of operations. Now, old earth (rock)-filled dams confront the following phenomena:

- rapid drawdowns and drawups of the water level in the dam reservoir (lake) and tailwater accompanied by fluctuations in the water content of dams' filling from dry, desiccated conditions to wet high pore-pressure ones,
- infiltration into the dam's body and riverbanks caused by torrential rains,
- surge waves and currents released through the dams' culverts and over the spillways, among others.

Seepage-induced/facilitated erosion of soil in earth (rock)-filled dams depends on dimensions of the embankment, its zonation (texture of the soil), and reservoir-tailwater levels. For example, piping, suffusion, and heaving (uplift) of the dam soil and parts of the constructed structure are controlled by seepage characteristics, mostly the hydraulic gradients and pore pressure [3, 16–18]. The criteria of stability against erosion are commonly developed and tested in simple column experiments, i.e., in well-controlled 1-D saturated seepage flow fields (see, for example, [12, 19–23]). Since seepage in real dams is transient, involves free and moving boundaries [24] of phreatic surfaces, and unsaturated zones above them, seepage flow (hydraulic gradients and pore pressures) needs to be characterized using mathematically complex 2-D or 3-D fields.

The geotechnical mitigation (forestalling) of seepage erosion is achieved via the construction of toe, chimney, blanket drains, and drainage galleries/tunnels inside the dam body and in the downstream berm, relief wells (vertical and horizontal), cutoff walls, sheet piling, grout curtains, cushioning of key embankment components by graded filter envelopes and geotextile wrapping, among others [25–35]. Some dam components (such as spillways) are added to the embankment long after the original design/construction, and therefore their impact on seepage in the dam may not be properly incorporated into the local/ overall analysis of the structure's stability, as Troyanowski [36] assessed and warned for dams' spillways.

The overall post-crisis opinion is that the collapse of the spillway was triggered by high-velocity overland flows occurring overexposed and un-engineered geologic surfaces. In this paper, we address a different factor: seepage near an impermeable barrier on the downstream slope of an earth dam that concurs with what France et al. [3] stated: *"A detailed study of the seepage flow under the slab would be necessary in this case to determine the uplift pressure distribution."*

The configuration of the Oroville Dam crisis is somewhat different than the idealized components of the problem addressed in this paper; in particular, we assumed the following:

- The dam body is a rectangular parallelepiped that makes possible conjugation of analytical and finite-element modeling.
- We ignore the herringbone drains under the slabs of the spillway [3].
- The spillway is a vertical rather than a tilted barrier.
- The barrier is impermeable to both seepage from the soil to the atmosphere and for leaks from the surface water into the soil subjacent to the spillway slabs; in other words, we do not study a coupled surface-subsurface flow which may have contributed to the crisis [3].
- Soil is homogeneous and isotropic.
- The lake stage in our models is also simplified as compared with the prototype dam.

France et al. [3] pointed out that no detailed analysis of seepage (in the report, called "groundwater flow") has been done by their forensic team. The main questions relevant to seepage are:

a) Can transient seepage with a phreatic surface, which propagates in a "pre-dried" embankment body, be a plausible cause of the collapse of an earthwork?
b) Can new analytical and numerical models of "global-scale" seepage through earth dams add better insights to what the classics [37, 38] posed as potential threats to dam stability?
c) How to connect these large (dam) scale seepage models to what is tested in column experiments with "core samples" of the embankment porous materials, subject to high and variable gradients (see, for example, [39])?
d) Can relatively fast external hydrological/hydraulic drivers, such as a rapid rise of the reservoir level or intensive rain, induce singular (ruinous) consequences via relatively slow seepage flows within the components of a porous dam?

2 Conceptualization of the flow problem

In our analysis, we consider Darcian, isothermic, single-phase, and incompressible water flow in a rigid porous skeleton (soil or rock-filling); saturated hydraulic conductivity k [m/s] and the van Genuchten–Mualem (VGM) soil hydraulic characteristics [40] are constant.

A physical 3-D domain is symmetric with respect to the barrier axis (Fig. 2a) and we study the right half of it. A system of Cartesian coordinates $x_1 x_2 y$ is centered at point A_1. An impermeable horizontal rectangle $A_1 A_2 D_3 D_1$ bounds the flow domain from below. The barrier is assumed to be an impermeable vertical rectangle $D_1 F_1 F_2 D_2$ placed on a vertical soil

Fig. 2 A schematic of 3-D phreatic flow through an earth dam (**a**), a vertical cross-section at $x_1=a$ (**b**)
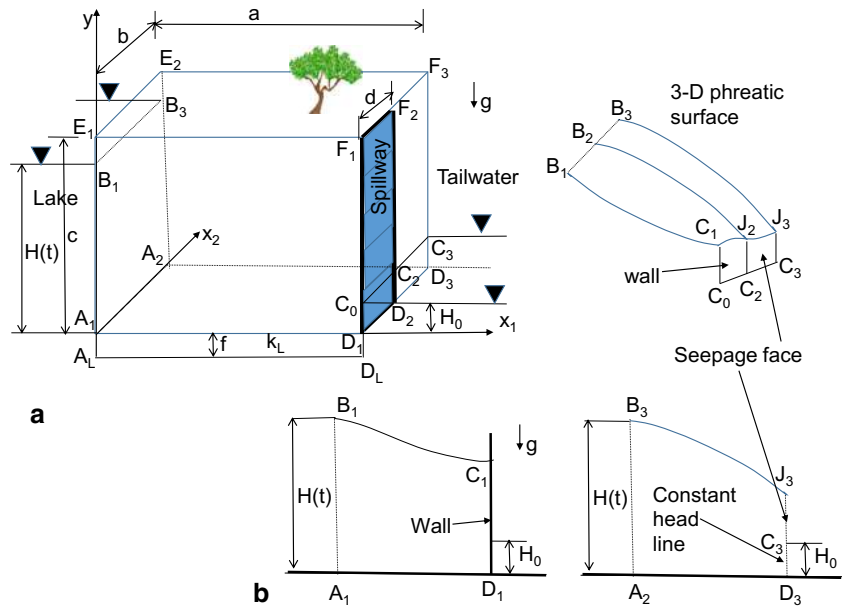
slope $D_1F_1F_3D_3$ that is an idealization of a spillway chute in Fig. 1.

We introduce the total hydraulic head $h(t, x_1, x_2, y)=p(t, x_1, x_2, y)+y$, where p is the pressure head. The reservoir water level $H(t)$ is rising such that the vertical face $A_1B_1B_2B_3A_2$ (the dam reservoir boundary) is under a time-variable condition in terms of h. The tailwater level H_0 is constant and, correspondingly, the total head h over the rectangle $D_2C_2C_3D_3$ is constant both in time and space. Through the horizontal rectangle $E_1E_2F_3F_1$ ($y=c$ in Fig. 2a) which represents the ground surface (a dam crest), rain recharges the water table.

The 3-D phreatic surface $B_1B_2B_3J_3J_2C_1$ (sketched in Fig. 2a) is affected by the barrier and outcrops at the tailwater vertical slope with a seepage face $J_3C_3C_2J_2$. A vertical cross-section $x_2=b$ in Fig. 2a depicts a phreatic line B_3J_3, with outflow through a seepage face segment C_3J_3 and a constant head segment D_3C_3. Another phreatic line, B_1J_1 is shown in a vertical cross-section $x_2=0$ (Fig. 2a) In this cross-section, the segment C_1D_1 is an impermeable wall and line of symmetry, i.e., the horizontal components of the Darcian velocity vector vanish there.

In 3-D, the rectangle $D_2J_2J_3D_3$ in Fig. 2a is a vent for outseeping water. The adjacent saturated soil is routinely viewed as a zone of the potential risk of seepage-induced erosion. However, despite Troyanowski's [36] warning, soil adjacent to the impermeable surface $D_1F_1F_2D_2$ (i.e., the under-chute soil) is seldom scrutinized for stability.

The trace of the 3-D phreatic surface $B_1B_2B_3J_3J_2C_1$ in the vertical plane $x_1=a$ is shown in Fig. 2b as curve $C_1J_2J_3$. The phreatic surface rises due to two drivers: the rise of the reservoir level $H(t)$ and accretion from the vadose zone. This creates the following threats to dam stability:

- A high pore pressure on the soil side of the barrier $D_1F_1F_2D_2$ creates a force perpendicular to this surface that can cause uplift-heaving of the concrete blocks and their jacking. Even small seepage-induced displacements of the blocks can be exacerbated by supercritical surface flow (shown in Fig. 1a) on the "external" (with respect to the porous medium) surface of the barrier.

- High vertical upward-oriented hydraulic gradients in the vicinity of point C_1 in Fig. 2b can cause dislodging and translocation of soil particles, especially, of the fine soil fraction under the spillway blocks; that reduces the block-soil grip.

- High lateral (in the x_2-direction) seepage gradients due to a phreatic mound due to the high variation of the elevation of the points on the curve $C_1J_2J_3$ in Fig. 2b can cause suffusion of soil under the barrier, as well as piping in the open (seepage face) zone of the tailwater. Clearly, without a barrier (concrete spillway) $C_1J_2J_3$ in Fig. 2b has a much milder slope and less threat of lateral suffusion.

Various analytical and numerical models have been used for studies of seepage in dam bodies (e.g., [41–53]). Below we follow the recommendation of Alvi [54] and use various mathematical models for determining 2-D and 3-D functions h and p, as well as hydraulic gradients within the dam.

In Section 3, we use the Dupuit-Forchheimer (DF) approximation and present a new analytical solution to the problem of a steady saturated flow occluded by the barrier (Fig. 2a). In Section 4, we revisit and further develop the Kacimov and Yakimov [55] analytical solution to a 2-D transient problem of a potential saturated flow with a phreatic surface rising in a capillarity-free soil. A vertical barrier occludes this rise. We

solve a moving boundary value problem (BVP) and calculate build-up of the seepage-induced pore pressure and hydraulic gradients. These analytical results are compared with HYDRUS [56] simulations for a saturated-unsaturated flow in soil with capillarity. There are no moving or free boundaries in HYDRUS. In Section 4, the HYDRUS model is used to simulate flow in a rectangular domain representing the dam's vertical cross-sections close to the plane $x_2=0$ (Fig. 2a). The phreatic line in HYDRUS is a zero-pressure isobar, which moves with the family of all other isobars.

In Section 5, we consider the early stage of the deluge when the earthwork is dry, and the drawup in the reservoir generates a saturated "tongue," which propagates inside of the dam. We consider a monotonic and non-monotonic reservoir hydrograph. The former is modeled using the Barenblatt analytical solution ([57]; referred to as PK-77) for capillarity-free soil on an impermeable foundation. For the latter, after a rapid rise of the reservoir level up to a peak stage, a relatively slow drawdown takes place (this is the actual situation in the Oroville lake when after February 2017 the reservoir level receded). We recur to the DF approximation and consider a transient nonlinear Boussinesq equation. Unlike in Section 3, we assume that the dam bed is a "leaky boundary", i.e., that it is made of a thin claylike stratum (aquitard shown as $A_LA_1D_1D_L$ in Fig. 2a), which transmits water down from the dam body. The Kalashnikov [58] analytical solution predicts that the saturated zone in a vertical cross-section is a right triangle, whose hypotenuse (a moving phreatic surface) tilts with an initially increasing and then decreasing slope.

The HYDRUS simulations are compared with the Kalashnikov solution at a time when the dynamics of pore water is controlled by the rise of the water level in the reservoir rather than the capillarity of the dam body and substratum. HYDRUS results are also compared with Barentblatt's solution, which is an exact one for both the Boussinesq equation and the 2-D potential model with a nonlinear phreatic surface boundary condition. HYDRUS reconstructs a perfectly prismatic saturated "tongue," which propagates from the reservoir into the dam at a constant rate of drawup.

In Section 6, we use HYDRUS to simulate a 3-D transient saturated-unsaturated flow in the entire box shown in Fig. 2a. These results (in the limit of constant H in Fig. 2a) are compared with the analytical solution in Section 6.

3 Analytical solution for vertically averaged steady flow impeded by a strip-barrier

In this Section, we neglect capillarity and flow transiency. We assume that the dam reservoir level is constant, i.e., $H(t)=H_1$=const. We also adopt the DF approximation (see PK-77, [1]) that eliminates the vertical coordinate y in

Fig. 2a, i.e., the total head $h(x_1,x_2)$ in the saturated zone coincides with the height $h_s(x_1,x_2)$ of a steady phreatic surface above the horizontal impermeable base $A_1A_2D_3D_1$. The impact of rain and the vadose zone on the saturated DF flow is accounted for through the recharge rate $N=const>0$ [m/s], which is space- and time-independent over the rectangle $E_1E_2F_3F_1$ (Fig. 3a). The analytical model below describes how DF flow "winds" (horizontally) around the impermeable barrier $D_1F_1F_2D_2$. Fig. 3a represents a planar view.

The water table position $h_s(x_1, x_2)$ and the discharge vector $\overrightarrow{F_S}(x_1, x_2)$ obey the following BVP in terms of Strack's potential (see, for example, [1, 59]):

$$
\begin{aligned}
&\overrightarrow{F_S} = \nabla\Phi, \\
&\nabla^2\Phi(x_1,x_2) = -N \\
&\Phi(0,x_2) = \Phi_1 = k\frac{H_1{}^2-H_0{}^2}{2} = const \ \text{ for } 0\leq x_2 \leq b, \text{ i.e. along } A_1A_2, \\
&\Phi(a,x_2) = 0 \text{ for } d\leq x_2 \leq b, \text{ i.e. along } D_2D_3, \\
&\frac{\partial\Phi}{\partial x_2}(x_1,b) = 0 \text{ for } 0\leq x_1 \leq a \text{ i.e. along } A_2D_3, \\
&\frac{\partial\Phi}{\partial x_2}(x_1,0) = 0 \text{ for } 0\leq x_1 \leq a \ i.e. along A_1D_1, \\
&\frac{\partial\Phi}{\partial x_1}(x_2,a) = 0 \ \text{ for } 0\leq x_2 \leq d \ i.e. \text{ along } D_1D_2
\end{aligned}
\tag{1}
$$

where $\Phi(x_1,x_2) = k\frac{h_s^2-H_0^2}{2}$ [m³/s] is the discharge potential, ∇ and ∇^2 are the gradient and Laplacian 2-D (i.e., in the plane x_1,x_2) operators. The vector $\overrightarrow{F_S}$ has components F_{x1} and F_{x2} along the corresponding axes (see Fig. 3a).

We decouple the solution to the BVP (1) in the following manner:

$$
\Phi = \Phi_P + \Phi_L
\tag{2}
$$

where the first term satisfies the BVP for the Poisson equation:

$$
\begin{aligned}
&\nabla^2\Phi_P(x_1,x_2) = -N \\
&\Phi_P(0,x_2) = \Phi_1 \text{ for } 0\leq x_2 \leq b, \text{ i.e. along } A_1A_2, \\
&\Phi_P(0,x_2) = 0 \text{ for } 0\leq x_2 \leq b, \text{ i.e. along } D_1D_3, \\
&\frac{\partial\Phi_P}{\partial x_2}(x_1,0) = \frac{\partial\Phi_P}{\partial x_2}(x_1,b) = 0 \text{ for } 0\leq x_1 \leq a, \text{ i.e. along } A_2D_3 and A_1D_1
\end{aligned}
\tag{3}
$$

The solution to the BVP (3) is trivial in 1-D:

$$
\Phi_P(x_1) = -N\frac{x_1^2}{2} + \left(\frac{Na}{2}-\frac{\Phi_1}{a}\right)x_1 + \Phi_1
\tag{4}
$$

From eq. (4), it follows:

$$
\frac{\partial\Phi_P}{\partial x_1} = -Nx_1 + \frac{Na}{2}-\frac{\Phi_1}{a}
\tag{5}
$$

The second term on the right-hand side (RHS) of eq. (2) is a harmonic function which satisfies the following BVP:

Fig. 3 The horizontal base 3-D flow domain in Fig. 2a and the rectangle in which Strack's potential is found (**a**), the domain of a fictitious flow and the boundary value problem for the harmonic component of Strack's potential (**b**), the hodograph domain of a fictitious flow (**c**), the complex potential domain of a fictitious flow (**d**), and an auxiliary half-plane (**e**)
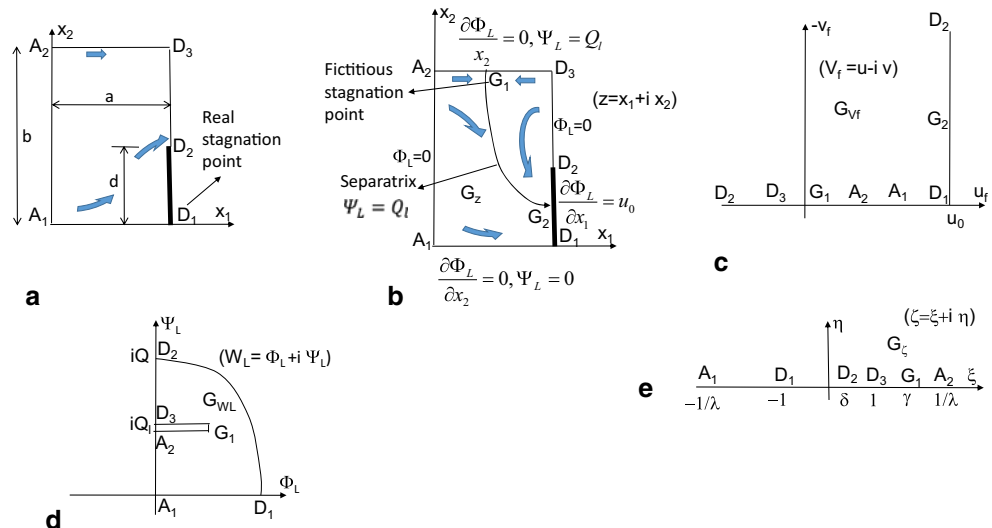
$$\nabla^2 \Phi_L(x_1, x_2) = 0$$
$$\Phi_L(0, x_2) = 0 \text{ for } 0 \leq x_2 \leq b, \text{ i.e. along } A_1 A_2$$
$$\Phi_L(0, x_2) = 0 \text{ for } d \leq x_2 \leq b, \text{ i.e. along } D_2 D_3,$$

$$\frac{\partial \Phi_L}{\partial x_2}(x_1, 0) = \frac{\partial \Phi_L}{\partial x_2}(x_1, b) = 0 \text{ for } 0 \leq x_1 \leq a, \text{ i.e. along } A_2 D_3 \text{ and } A_1 D_1$$
$$\frac{\partial \Phi_L}{\partial x_1}(a, x_2) = -\frac{\partial \Phi_P}{\partial x_1}(a, x_2) = \frac{Na}{2} + \frac{\Phi_1}{a} = u_0 \text{ for } d \leq x_2 \leq b, \text{ i.e. along } D_1 D_2$$

$$(6)$$

The last boundary condition for $\frac{\partial \Phi_L}{\partial x_1}(a, x_2)$ in eq. (6) follows from eq. (5). For Φ_L, eq. (6) thus states a mixed BVP (see the details of this type of BVPs in PK-77). We use the hodograph method to solve this BVP. Namely, we consider Φ_L as a potential of a fictitious pseudo-flow with a velocity $\overrightarrow{V_f} = \nabla \Phi_L$, a vector having a horizontal component u_f and a vertical component v_f. Then the complex function $V_f = u_f - iv_f = dW_L/dz$ is holomorphic in the complex plane $z = x_1 + ix_2$ (the corresponding domain G_z is shown in Fig. 3b). The function $W_L = \Phi_L + i\Psi_L$ is a complex potential of the pseudo-flow. Ψ_L is a stream function of the pseudo-flow. It is harmonic and conjugated with Φ_L via the Cauchy-Riemann conditions. The mirrored hodograph domain is a right angle G_{Vf}, which is shown in Fig. 3c, u_0 is a given (see eq. 6) positive constant. We note that the point G_1 in G_{Vf} is a stagnation point of the fictitious flow; the real flow, which is quantified by the full Strack potential Φ, has D_1 as a stagnation point (compare Fig. 3a, b). The separatrix $G_1 G_2$ divides the pseudo-flow into a part, which feeds $D_1 D_2$ by the segment $D_2 D_3$, from one emanated from $A_1 A_2$. The complex potential domain, G_{WL}, corresponding to G_z, is depicted in Fig. 3d. G_{WL} has a horizontal cut $A_2 G_1 D_3$ along which $\Psi_L = Q_l$ that is the pseudo-flow rate from $A_1 A_2$ into $D_1 G_2$. The total pseudo-flow rate into $D_1 D_2$ is Q. The pseudo-flow rate from $D_2 D_3$ into $D_2 G_2$ is $Q_r = Q - Q_l$. It is noteworthy that the scalars

Q, Q_l, and Q_r are to be found. Both the real flow in Fig. 3a and fictitious flow in Fig. 3b have a singularity at point D_2 where both the Strack discharge vector $\overrightarrow{F_S}(a, d)$ and the fictitious velocity $\overrightarrow{V_f}(a, d)$ blow up.

We introduce an auxiliary variable $\zeta = \xi + i\eta$ and map conformally the half-plane G_ξ: $\xi > 0$ (Fig. 3e) onto G_z by the Shwartz-Christoffel function:

$$z = ic_1 \int_{-1/\lambda}^{\zeta} \frac{d\tau}{\sqrt{(1 - \lambda^2 \tau^2)(1 - \tau^2)}} \quad (7)$$

where the branch of the root is fixed in such a manner that the root is positive at $\zeta = \xi$, $\eta = 0$, $-1 < \xi < 1$. The mapping constant is determined from the given width of G_z, $z(-1) = a$, $c_1 = a/K'$, where K' is the complete elliptic integral of the first kind with the modulus $\sqrt{1 - \lambda^2}$. We know the height of G_z in Fig. 3b. Therefore, the relation $z(1) = a + ib$ in eq. (7) gives:

$$\frac{b}{a} = \frac{2K}{K'} \quad (8)$$

where K is the complete elliptic integral of the first kind with the modulus λ. From eq. (8) we find the value of λ by the **FindRoot** and **EllipticK** routines of Wolfram's [60] *Mathematica*.

From eq. (7) the affix δ of point D_2 in G_ζ (Fig. 3e) is:

$$d = \frac{a}{K'} \int_{-1}^{\delta} \frac{d\tau}{\sqrt{(1 - \lambda^2 \tau^2)(1 - \tau^2)}} \quad (9)$$

Equation (9) is a nonlinear equation with respect to δ, which we again solve by the **FindRoot** routine of Wolfram's *Mathematica*.

Next, we map conformally G_ζ onto the quadrant G_{Vf} (Fig. 3b) by the Shwartz-Christoffel function:

$$V_f = \frac{dW_L}{dz} = c_2 \int_{-1}^{\zeta} (\tau - \delta)^{-3/2} (\tau + 1)^{-1/2} d\tau + u_0$$

$$= -\frac{2c_2}{(1+\delta)} \sqrt{\frac{1+\zeta}{\zeta-\delta}} + u_0 \qquad (10)$$

where the branch of the root is selected positive along the ξ-axis in Fig. 3e, in the interval $\xi > \delta$ (and therefore at $\xi < -1$). The mapping constant c_2 will be found later. Obviously, in the interval $-1 < \xi < \delta$, the root in eq. (10) is imaginary (see the ray D_1D_2 in Fig. 3c). From eq. (10), the singularity at point D_2 is $V_f \sim (\zeta - \delta)^{-1/2}$ that can be expressed via $\zeta(z)$ from eq. (7). Obviously, $z(\zeta)$ is regular at point D_2.

We assume that point A_1 is fiducial, i.e., at this point $W_L = 0$ (the complex potential is defined up to an arbitrary complex constant, see PK-77). Then

$$W_L = \int_{-1/\lambda}^{\zeta} \frac{dW_L}{dz}(\tau) \frac{dz}{d\tau}(\tau) d\tau \qquad (11)$$

By using eqs. (10) and (7) in the integrand of eq. (11) we get

$$W_L = u_0 z(\zeta) - i \frac{2ac_2}{K'(1+\delta)} \int_{-1/\lambda}^{\zeta} \frac{d\tau}{\sqrt{(\tau-\delta)(1-\tau)(1-\lambda^2\tau^2)}} \qquad (12)$$

Now we determine c_2 from the condition at the point $\xi = \delta$ where $z = a + id$ and $W_L = iQ$.

From the last line in eq. (6) we have a constant horizontal pseudo-velocity $\frac{\partial \Phi_L}{\partial x_1} = u_0$ along D_1D_2 and therefore $Q = u_0 * d$. Then, from eq. (12) we get

$$u_0 a = \frac{2ac_2}{K'(1+\delta)} \int_{-1/\lambda}^{\delta} \frac{d\tau}{\sqrt{(\delta-\tau)(1-\tau)(1-\lambda^2\tau^2)}} \qquad (13)$$

From eq. (13) we immediately express c_2 and put it back into eq. (12) which becomes

$$W_L = u_0 z(\zeta) - i \frac{au_0}{I_1} \int_{-1/\lambda}^{\zeta} \frac{d\tau}{\sqrt{(\tau-\delta)(1-\tau)(1-\lambda^2\tau^2)}}, \quad I_1$$

$$= \int_{-1/\lambda}^{\delta} \frac{d\tau}{\sqrt{(\delta-\tau)(1-\tau)(1-\lambda^2\tau^2)}} \qquad (14)$$

We separate the real part in eq. (14) and get Φ_L. Then, we re-assemble eqs. (11) and (4) to get the final solution in terms of Strack's potential (2).

We introduce dimensionless variables by normalizing all geometrical sizes to a and the Darcian velocity to k.

The parametric equation of the phreatic curve C_1J_2 (Fig. 2b) is:

$$h_{sw}(\xi) = \sqrt{(H_1^2 - H_0^2)\left(1 - \frac{1}{I_1} \mathrm{Re} \int_{-1/\lambda}^{\zeta} \frac{d\tau}{\sqrt{(\tau-\delta)(1-\tau)(1-\lambda^2\tau^2)}}\right) + H_0^2},$$

$$x_2(\xi) = \frac{K + F(\arcsin\xi, \lambda)}{K'}, \qquad -1 < \xi < \delta \qquad (15)$$

where F is the incomplete elliptic integral of the first kind. Similarly, from (7) and (14) we get parametric equations of B_1C_1 as $h_{ss}(\xi), x_1(\xi), -1/\lambda < \xi < -1$.

Suffusion, piping, and lessivage are controlled by the vector of the hydraulic gradient (PK-77) $\vec{J} = \vec{V}/k$. In the DF model, while $\vec{J}$ does not vary with y, it varies with x_1 and x_2 as follows:

$$\vec{J} = -\nabla h_s(x_1, x_2) \qquad (16)$$

In eq. (16), $\vec{J}$ has components J_{x1} and J_{x2} in the x_1 and x_2 directions, respectively. For example, from eq. (15) along the barrier $J_{x1} = 0$ and the component of the magnitude of J_{x2} is:

$$J_{x2w}(\xi) = \left| \frac{d[h_{sw}(\xi)]}{d\xi} \left(\frac{d[x_2(\xi)]}{d\xi}\right)^{-1} \right|, x_2(\xi)$$

$$= \frac{K + F(\arcsin\xi, \lambda)}{K'}, \qquad -1 < \xi < \delta \qquad (17)$$

In computations involving eqs. (15) and (17), we used the *Mathematica* routines **NIntegrate**, **EllipticF**, and **ParametricPlot**. Figure 4a, b, c shows $h_{sw}(x_2), J_{x2w}(x_2),$ and $h_{ss}(x_1)$ for dimensionless parameters $b=4$, $d=3/15$, $H_1=102/50$, $H_1=2/50$, and $N=0$ (see also Figs. 2a and 3a for the corresponding points). The choice of these quantities is connected to ones in numerical simulations of Section 6 below. Figure 4a and b show a steep drop of the phreatic surface from point C_1 to J_2 and extremely high gradients, especially, close to the rim of the barrier, D_2J_2. These gradients well exceed the safe limit of PK-77, which is $|\vec{J}| = 1$.

For assessments of heaving (uplifting) of the barrier blocks, we introduce a dimensionless (normalized to $\rho g a$, where ρ is the density of water) integral pore pressure acting on the barrier:

$$P_i = \int_0^d \int_0^{h_s(1,x_2)} (h_s(1,x_2) - y) dy dx_2 = \int_0^d \frac{[h_s(1,x_2)]^2}{2} dx_2$$

$$= \int_{-1}^{\delta} \frac{[h_{sw}(\xi)]^2}{2} \frac{dx_2(\xi)}{d\xi} d\xi \qquad (18)$$

i.e., an integral of the pore pressure over a curvilinear trapezium $D_1C_1J_2D_2$ (Fig. 2b). This trapezium is the "wetted area" of the barrier, "submerged" under the phreatic surface. The force (normalized to the specific weight of pore water and

Fig. 4 **a** The phreatic curve C_1J_2
for dimensionless parameters
$b=4$, $d=3/15$, $H_1=102/50$, $H_1=2/50$, $N=0$. **b** The hydraulic gradient
along the barrier for
dimensionless parameters $b=4$,
$d=3/15$, $H_1=102/50$, $H_1=2/50$,
$N=0$. **c** The phreatic curve B_1C_1
for dimensionless parameters
$b=4$, $d=3/15$, $H_1=102/50$, $H_1=2/50$, $N=0$
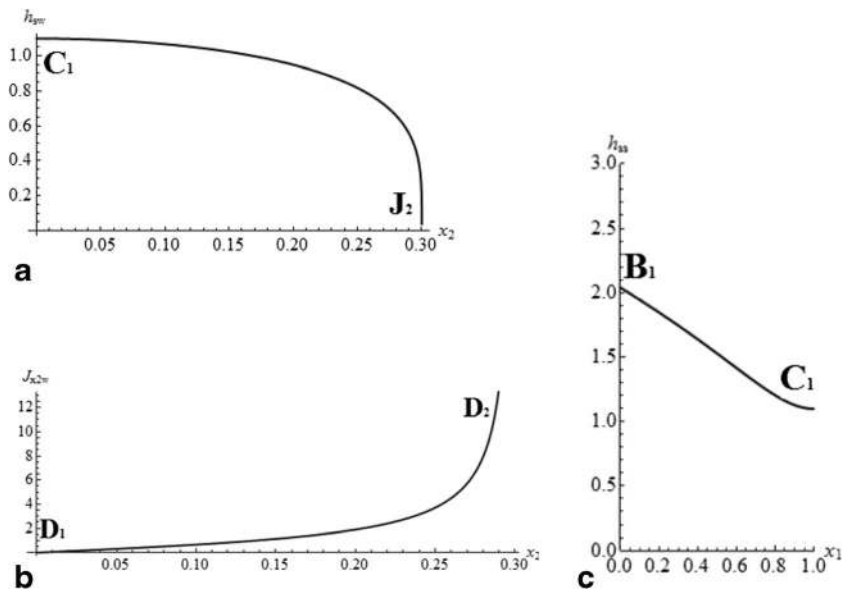
a) due to the hydrostatic pressure is $F_i = P_i/Ar$, where Ar is the "sub-phreatic" (wetted) area of $D_1C_1J_2D_2$. For the example illustrated in Fig. 4, computations give $P_i=0.14$ and $F_i=0.49$. Similarly, we can find the center of the seepage pressure exerted on $D_1C_1J_2D_2$. If the barrier consists of blocks, then the seepage force acting on a block, the point of its application, and the force moments, which are needed for assessing the threat of jacking, can be easily found by integrations similar to eq. (18).

4 Transient 2-D flow in a vertical plane, for a constant-rate drawup

In this section, we consider a transient element of 3-D flow in Fig. 2a, i.e., seepage in the vertical plane $x_2=0$. Figure 5 a shows the vertical cross-section x_1A_1y, in which we introduce Cartesian coordinates XY with the origin at a moving point C_1 where the rising phreatic surface intersects the vertical barrier. Although the real 3-D phreatic surface drops from C_1 to the rim of the barrier (point J_2 in Fig. 2a), in this Section we assume that the barrier half-width d is high enough so that we can assume flow to be 2-D in the plane XY, i.e., close to the line D_1C_1 in Fig. 2a.

4.1 Analytical similarity solution for phreatic flow impeded by a vertical barrier

The water level in the dam reservoir rises with time t [days] at a constant rate R [m/day]. We assume that this rise continues for a sufficiently long time such that the phreatic line B_1C_1 propagates in a porous slab of a width a as a traveling wave, i.e., without any change in its shape (see details of the corresponding similarity solution in [55]). This regime is realized if the impermeable bed $A_1A_2D_3D_1$ is far beneath B_1C_1, i.e., $H(t)$ in Fig. 2a is high enough. Correspondingly, the base A_1D_1 is

not even shown in Fig. 5a. Then, we can ignore $A_1A_2D_3D_1$ and study flow in a half-strip AB_1C_1, where A is an "infinity point." A rising curve B_1C_1 caps the domain G_z in Fig. 5a. The difference in elevations of points B_1 and C_1, the depth, tr, of this advancing "trough" on the phreatic line is a part of the solution.

Similarly to Section 2, the stability of C_1A against seepage-induced erosion is controlled by the distribution of the pore pressure head $p(X,Y,t)$ and the Darcian velocity $\overrightarrow{V} = -k\nabla h(X, Y, t)$, especially, in the vicinity of $Y=0$, i.e., close to the point C_1 in Fig. 5a. In the following text, we work in a system of coordinates, which translates upwards with a speed R.

In the analytical solution below, we neglect accretion on the phreatic surface and capillarity of the soil, i.e., assume a piston type rise (or imbibition, see [61]) of B_1C_1. This means that the soil beneath this line is saturated and above it is dry, with an instantaneous saturation occurring when B_1C_1 passes through this point. The porosity of the soil is $휏_s$ and the irreducible moisture content is $휏_r$ (in the analytic solutions below we assume $휏_r=0$).

Due to symmetry, we can mirror the physical strip G_Z about the C_1Y axis that results in an "image reservoir" on the right of the barrier (Fig. 5a). Point B_m is a mirror image of point B_1. We introduce a complex physical coordinate $Z=X+iY$. The complex coordinates of points B_1 and B_m are $\mp a + i\, tr$, correspondingly.

Similarly to Kacimov and Yakimov [55], we introduce a complex potential $w = \phi + i\psi, \phi = -kh$ and a function $V_c=dw/dZ$, which is complex-conjugated with the complexified Darcian velocity $V=u+iv$, i.e., $V_c=u-iv$ where u and v are, correspondingly, the X and Y components of the Darcian velocity vector $\overrightarrow{V}$. The domain G_{Vc} is a circular digon (a lune-shaped polygon) shown in Fig. 5b. The curve $B_mC_1B_1$ is an

Fig. 5 A rising phreatic surface in the vertical cross-section x_1A_1y (Fig. 2a) with a baffling vertical barrier (**a**), a hodograph domain (**b**), a domain in the complex potential plane (**c**), and a reference half-plane (**d**)
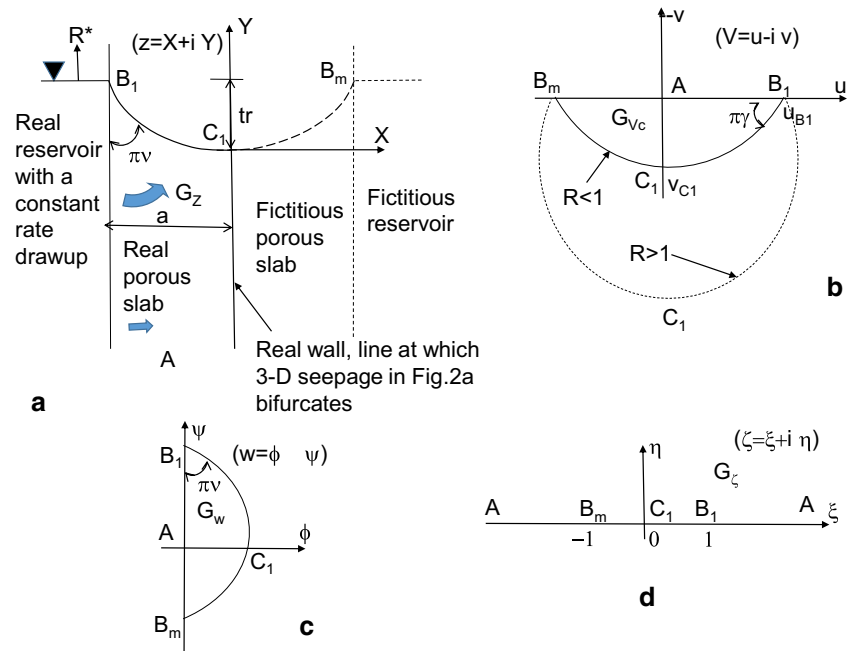
arc of a circle of a radius $(k + \theta_s R)/2$, centered at a point $i \cdot (k - \theta_s R)/2$ and at an angle $\pi\gamma$ with the u-axis. Darcian velocities at points B_1 and C_1 are horizontal and vertical with magnitudes u_{B1} and v_{C1}, respectively. We select point A as fiducial, i.e., $w_A=0$. Then, the complex potential domain G_w, shown in Fig. 5c, is a digon with an angle πv between the phreatic surface and the coordinate axis.

We introduce dimensionless variables $(z*, X*, Y*, h*, tr*) = (z, X, Y, h, tr)/a$, $(V*, u_{B1}^*, v_{C1}^*) = (V, u_{B1}, v_{C1})/k$, $(w*, \phi^*, \psi^*) = (w, \phi, \psi)/(k*a)$, and $R* = q_s R/k$. For the sake of brevity, we drop the superscript "*". Kacimov and Yakimov [55] obtained the shape of B_1C_1 and found that $u_{B1} = \sqrt{R}$; $v_{C1} = R$; $\cot(\pi v) = \sqrt{R}$; $\gamma = 1 - 2 \cdot v$ (see also the phreatic surfaces in Fig. 5a of [55]). We note that if $R>1$ then the center of the circle $B_1C_1B_m$ in the V_c-plane is below the u_c-axis and $\gamma>1/2$ (Fig. 5b, dashed line).

Kacimov and Yakimov [55] introduced an auxiliary variable $z = x + i \times h$ and considered a reference half-plane G_ζ, $-\infty < \xi < \infty$, $\eta > 0$, $\zeta = \xi + i\eta$ (Fig.4.1d) onto which G_z has been mapped by the function, which is obtained by integration of the following function:

$$\Xi(\zeta) = \frac{dZ}{d\zeta} = \frac{i}{\pi}\left[\frac{e^{v\pi i}}{(1+\zeta)^v \cdot (1-\zeta)^{1-v}} - \frac{e^{-v\pi i}}{(1+\zeta)^{1-v} \cdot (1-\zeta)^v}\right] \quad (19)$$

Now, we use the PK-77 method for determination of the function $\Omega(\zeta) = \frac{dw}{d\zeta}$, where $w(\zeta)$ is the complex potential as a function of ζ:

$$\Omega(\zeta) = \frac{i \cdot \sqrt{R}}{\pi}\left[\frac{e^{n\pi i}}{(1+\zeta)^v \cdot (1-\zeta)^{1-v}} + \frac{e^{-n\pi i}}{(1+\zeta)^{1-v} \cdot (1-\zeta)^v}\right] \quad (20)$$

Consequently, for $V_c = \frac{dw}{dZ} = \frac{\Omega}{\Xi}$ from eqs. (19)-(20), we obtain:

$$V_c(\zeta) = \sqrt{R}\frac{(1 + \zeta)^\gamma \cdot e^{v\pi i} + (1-\zeta)^\gamma \cdot e^{-v\pi i}}{(1 + \zeta)^\gamma \cdot e^{v\pi i} - (1-\zeta)^\gamma \cdot e^{-v\pi i}} \quad (21)$$

Then, integration of eqs. (19)-(20) yields:

$$tr = \mathrm{Im}\left(\int_0^1 \Xi(\tau)\,d\tau\right) = \frac{1}{i}\int_0^1 \Xi(\tau)\,d\tau + 1$$
$$Y(\eta) = \mathrm{Im}\left(\int_0^{i\cdot\eta} \Xi(\tau)\,d\tau\right) = \frac{1}{i}\int_0^{i\cdot\eta} \Xi(\tau)\,d\tau, \quad 0 \leq \eta < \infty, \quad 0 \geq Y > -\infty$$
$$h(\eta) = -tr + \int_0^{i\cdot\eta} \Omega(\tau)\,d\tau, \quad 0 \leq \eta < \infty, \quad -tr < h < 0$$
$$v(\eta) = i \cdot V_c(i\cdot\eta) \quad 0 \leq \eta < \infty, \quad R < v_y < 0 \quad (22)$$

From eq. (22), the distribution of the pore pressure along AC_1 is obtained as a parametric equation:

$$Y = Y(\eta), \quad p(\eta) = h(\eta) - Y(\eta) + tr, \quad 0 \leq \eta < \infty \quad (23)$$

Similarly, the distribution of the velocity along AC_1 is determined from eq. (22) by the parametric equation:

$$Y = Y(\eta), v = v(\eta), \quad 0 \leq \eta < \infty \quad (24)$$

Figure 6 presents computations based on eqs. (22)-(24), which we carried out in Wolfram's *Mathematica* for three dimensionless drawup rates, $R=4$, 1, and 0.25. The corresponding curves 1v-3v are the Darcian vertically-oriented velocities $v(-Y)$ along C_1A in Fig. 5a; the curves 1h-3h show the vertical distribution of the total hydraulic head $h(-Y)$ along the barrier and the curve 1p is the distribution of the pore pressure for $R=4$. These results illustrate that at dimensionless depths of
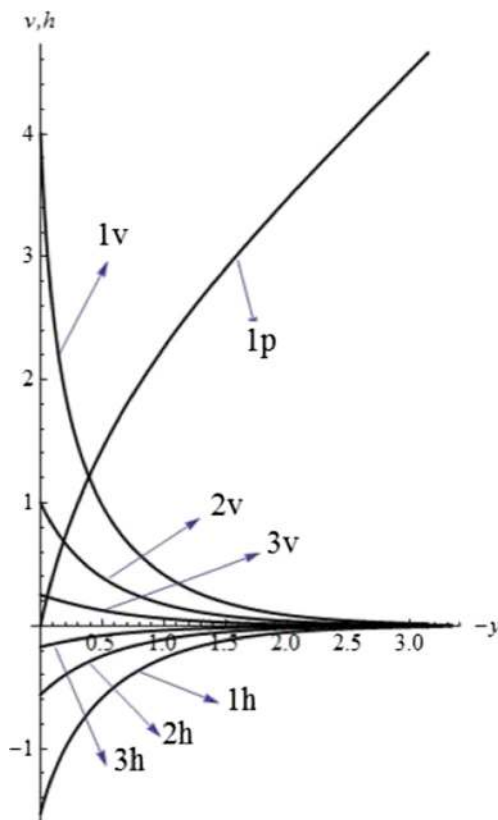
Fig. 6 Darcian velocities v (curves 1v-3v are for dimensionless drawup rates $R=4, 1, 0.25$, respectively), the total hydraulic head h (curves 1h-3h are for $R=4, 1, 0.25$, respectively) and the pore pressure p (for $R=4$) along AC_1 in Fig. 5a

$Y \sim -3$, water close to the barrier is almost stagnant, the total head is almost the same as in the reservoir, and the pore pressure is almost hydrostatic. However, closer to the rising phreatic surface (point C_1 in Fig. 5a), the hydraulic gradients are high, i.e., in this zone the soil adjacent to the barrier is temporary, when the traveling phreatic line B_1C_1 passes through, susceptible to erosion.

4.2 HYDRUS solution in a rectangle with an impeding vertical barrier

For comparisons, in this Subsection, we return to dimensional quantities and use HYDRUS [56] to simulate a transient 2-D saturated-unsaturated flow in a rectangular domain with a vertical barrier, similar to C_1A in Fig. 5a. We consider drawup for $0 < t < 7$ days with a rate of $R = 50$ cm/day. Below we use the HYDRUS notations and coordinates (X_H, Z_H) with the origin of coordinates at point A_1 (Fig. 2a). The rectangle $A_1E_1F_1D_1$ of sizes $a=100$ cm and $c=450$ cm in X_H and Z_H directions, respectively, is shown in Fig. 7.

First, we selected loam as the dam material, for which we retrieved the physical properties from the HYDRUS Soil Catalogue, i.e., $k=25$ cm/day, $\theta_s=0.43$, $\theta_r=0.078$, and the Vedernikov and Bouwer [40] constants $\alpha=0.036$ cm^{-1} and

$n=1.56$. In the analytical solution, the corresponding dimensionless drawup rate is 0.71.

The transport domain was discretized into finite elements with the following parameters and/or statistics: a targeted size of finite elements of 2.5 cm, 11,771 nodes, 440 1-D and 23,100 2-D finite elements. We assumed that prior to the reservoir filling and a seepage event (at $t=0$) the whole rectangle was dry with an initial pressure head of $p_d=-10,000$ cm. The boundary conditions were selected as follows. No flow was assumed along the three sides of the rectangle, A_1D_1, D_1F_1, and F_1E_1. Along the "expanding" boundary segment A_1B_1, water level in the reservoir rises and a time-variable boundary condition with a linear increase of the pressure head $p(0, Z, t)$ with time for Z varying from point A_1 (fixed) to point B_1 (moving) was specified. In other words, the total head h along A_1B_1 was constant at any fixed time instance and was increasing linearly as a function of time. The "shrinking" vertical segment B_1E_1 was assumed to be impermeable because the pressure head there was negative. This boundary condition is consistent with one in the analytical model of Vedernikov and Bouwer [63].

Figures 7 a, b, c, d, and e show colored plots of $p(X, Z, t)$ for time instances $t=1, 2, 3, 4$, and 7 days. The similarity regime, examined in the analytical solution (Fig. 5), is indeed established after about 3 days. From Fig. 7a and a boundary line chart $p(X, 0, 1)$ generated by HYDRUS we obtain that at $t=1$ day the tip, W_B, of the phreatic surface is at the locus $X_{Wn}=76$ cm. The isotachs $V=const$ are shown in Figs. 7f–g at time $t=7$ days. These isolines demarcate a "tongue" of high hydraulic gradients (their magnitude exceeds 2 near point B_1) close to the reservoir boundary. It is geotechnically worrisome that, for example, at $t=7$ days (Fig. 7f), a zone of gradients of magnitude higher than 0.1 extends more than 100 cm beneath the phreatic surface. Fig. 7g shows the contour lines of horizontal components, u, of the Darcian velocity vector plotted at $t=7$ days. The magnitude of velocity at point C_1 is $V_{C1} \approx 16$ cm/day. The analytical solution from Subsection 4.1 gives the corresponding value of $V_{C1} = 21.5$ cm/day when $\theta_s=0.43$ is used in the definition of the linear average velocity and $V_{C1} = 17.6$ cm/day when the porosity is replaced by an "effective" value, $\theta_e = \theta_s - \theta_r = 0.43-0.078$, i.e., $V_{C1}=\theta_e*R$. The depth of the trough (Fig. 5a) obtained by HYDRUS is $tr \approx 39$ cm as compared with those obtained by the analytical solution, viz. $tr =$

Fig. 7 The results of the HYDRUS computations for a constant rate of ▶ drawup in a rectangle made of loam ($k=25$ cm/day, $\theta_s=0.43$, $\theta_r=0.078$, $\alpha=0.036$ cm^{-1}, and $n=1.56$; $R=50$ cm/day, the initial pressure head $p_d=-10000$ cm) (**a-g**) and sand ($k=0.495$ cm/min, $\theta_s=0.43$, $\theta_r=0.045$, $\alpha=0.145$ cm^{-1} and $n=2.68$; $R=25$ cm/min, the initial pressure head $p_d=-100$ cm) (**h-i**). The pressure heads are displayed in (**a-e**) and (**h**); water fluxes in (**f**), (**g**), and (**i**).
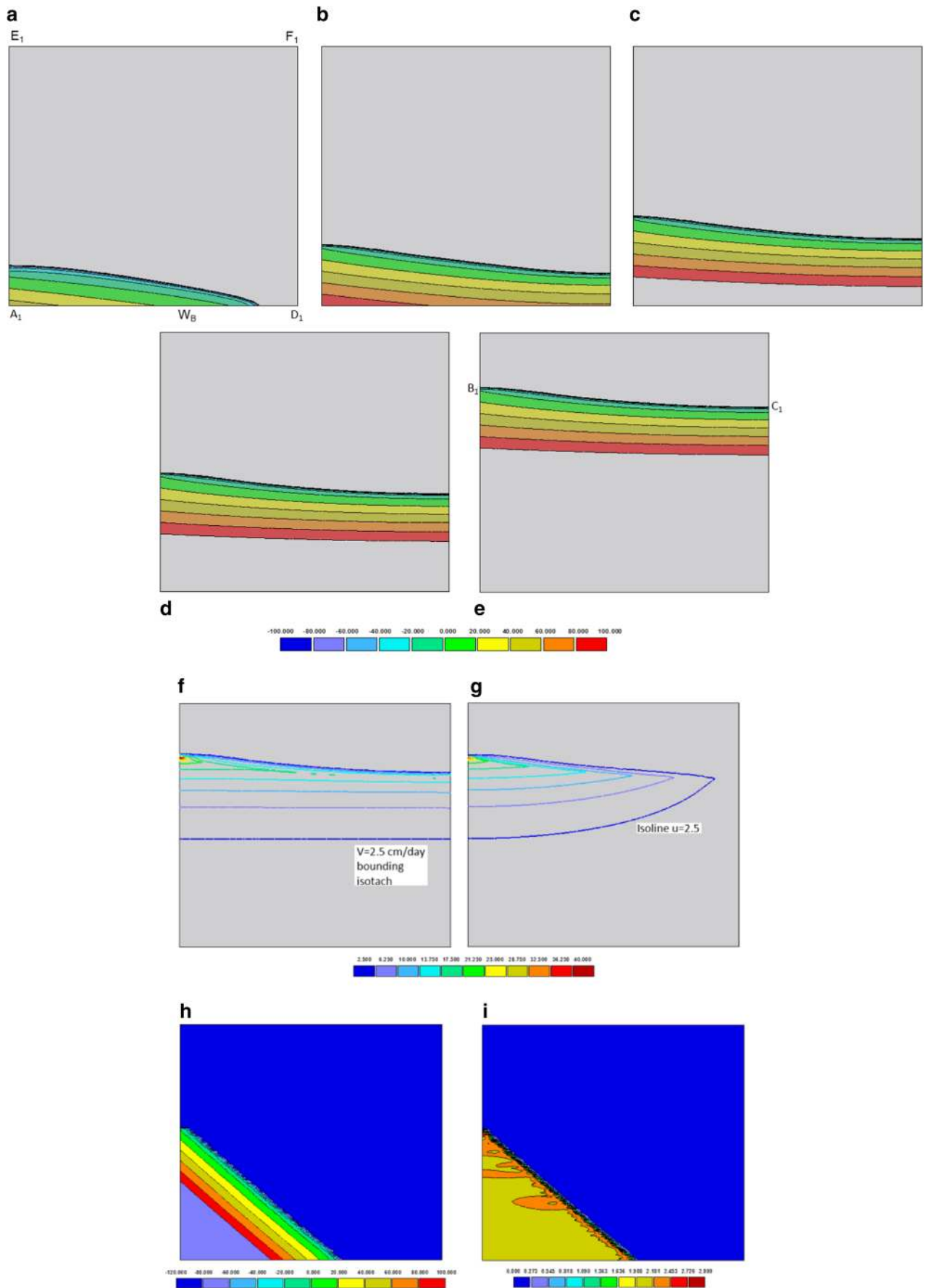
49.72 *cm* and $tr = 42.19$ *cm*, depending on whether 휀$_s$ or 휀$_e$ is used in the definition of velocity.

4.3 The Barenblatt's analytical solution versus HYDRUS simulations for the "saturated tongue" without a barrier impedance

The difference between the analytical and HYDRUS results is reduced when the two models physically converge, i.e., when the impact of soil's capillarity is minimized. In this subsection, we consider the same dam geometry as in Fig. 7a-g, but with the dam material being sand (휀$_s$=0.43, 휀$_r$=0.045, and the van Genuchten [40] constants 훾=0.145 cm^{-1} and n=2.68, k=0.495 cm/min). In this case, capillarity plays a relatively minor role in the Richards equation. We assume that the reservoir level rises with a rate of R =25 cm/min, the initial pressure head in the rectangle is p_d=-100 cm (this is very dry for sand).

Barenblatt (see PK-77 for full details) obtained another analytical similarity solution for the problem of a "linear drawup" of the reservoir water level with the propagation of a wetting front into a dry dam without capillarity at relatively small values of t, when the "saturated tongue" does not reach the confining (right) barrier (D$_1$F$_1$ in Fig. 2a) at the other end of the domain. In Barenblatt's solution, the dimensional Darcian velocity, $u_a = \sqrt{k\,R\,\theta_s}$, is purely horizontal and constant in the entire flow domain. The time-expanding saturated domain is exactly a right triangle, the hypotenuse of which is a "tilted" phreatic surface with a constant slope. The locus of the front, i.e., the intersection of the phreatic line with the impermeable base of the dam (D$_1$A$_1$ in Fig. 2a) is $X_{Wa}(t) = t\sqrt{k\,R/\theta_s}$. It is noteworthy that Barenblatt's "expanding triangle" is an exact solution to both the Laplace equation in a potential transient 2-D flow model and to the Boussinesq 1-D equation, which is based on the DF approximation.

HYDRUS isobars and isotachs for the selected example are shown in Fig. 7h and i, respectively. The position of the front after 10 min of flooding is $X_{Wn} \approx 56$ cm (Fig. 7h) according to HYDRUS, and X_{wa}=53.9 cm and 59.6 cm according to the Barenblatt analytical solution, depending on the choice of porosity or "effective" porosity, respectively. At the same time, the magnitude of velocity, although not exactly constant, in the bulk of the rectangular trough is $u_n \approx 2$ cm/min according to the numerical solution (Fig. 7i) and u_a=2.3 cm/min and 2.1 cm/min according to the Barenblatt analytical solution, depending on whether θ_s or θ_e is used, respectively. These comparisons cross-verify that the phreatic surface model based on the analytical solution and the numerical solution of the Richards equation provide similar results. This substantiates a combined utilization of HYDRUS and analytical models.
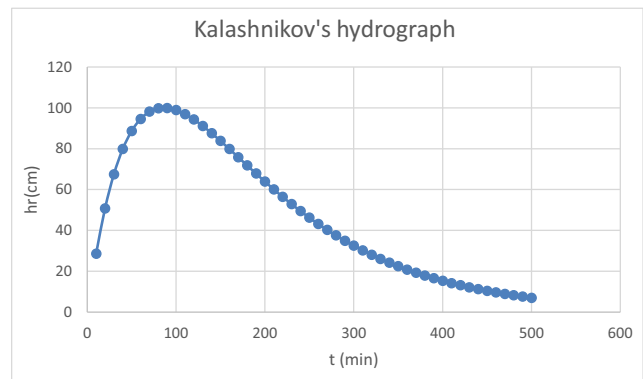

Fig. 8 Kalashnikov's one-peak hydrograph

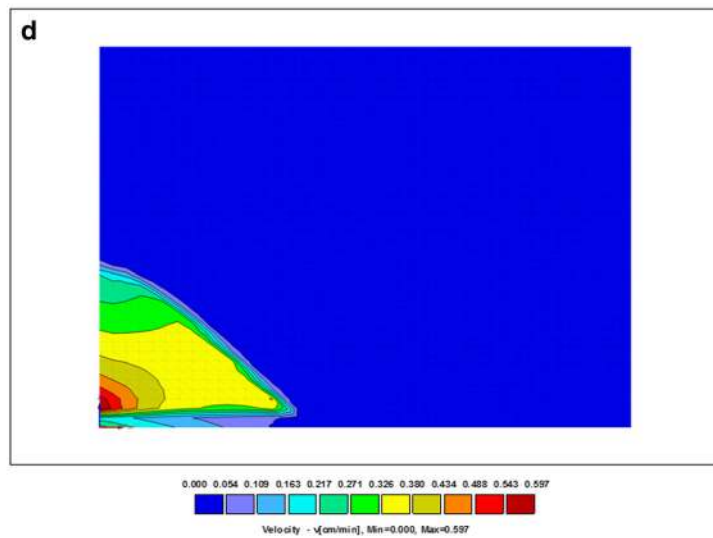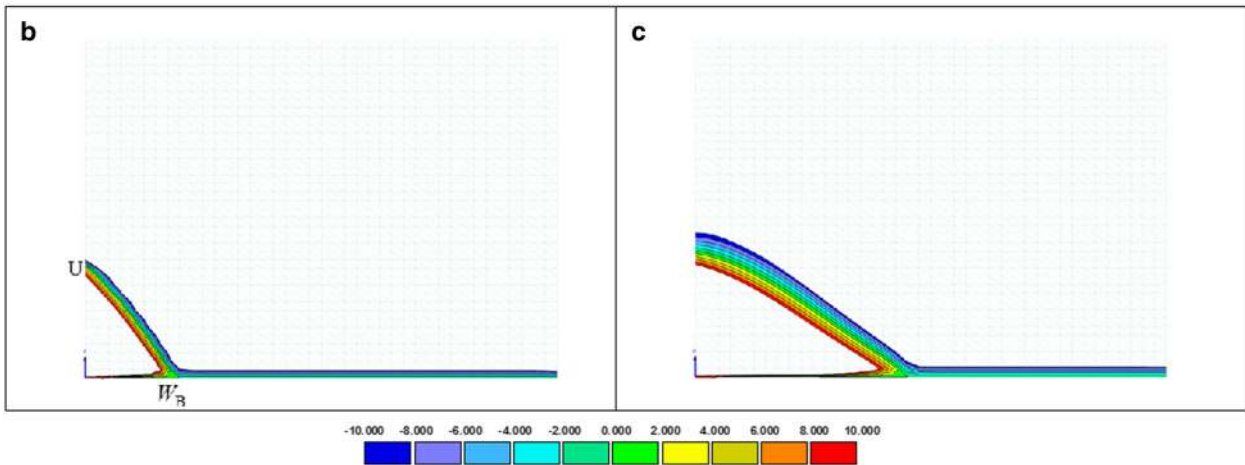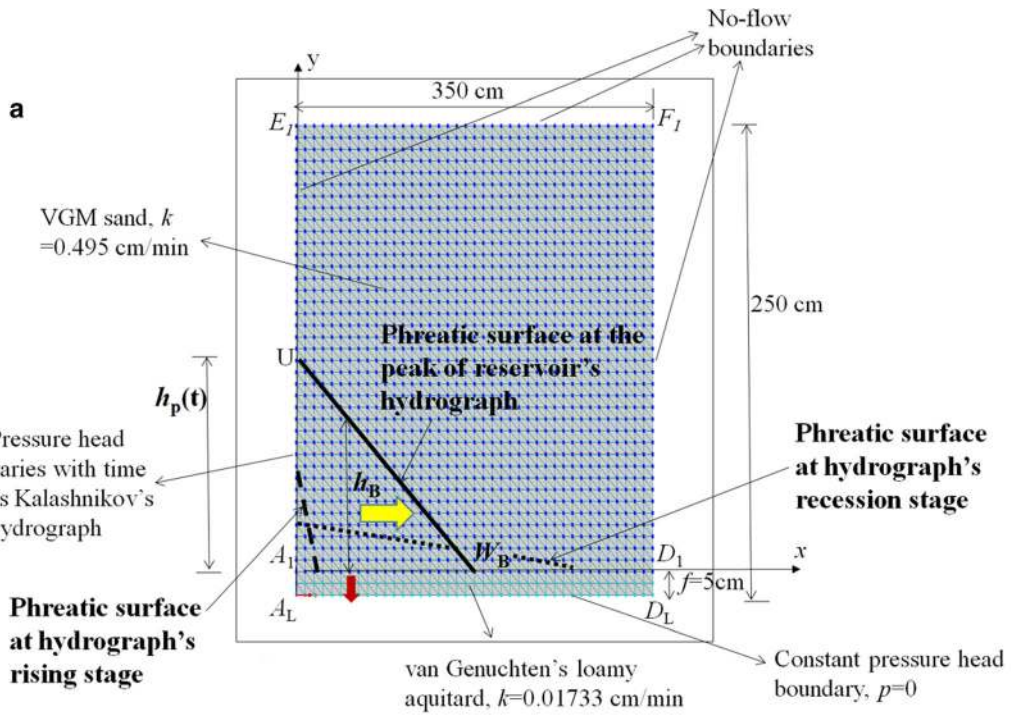## 5 Transient 2-D flow, drawup-drawdown hydrograph

A typical hydrograph (see, for example, Fig. 8), especially for recharge dams in Oman [64], is a one peak curve, which rapidly rises from a zero-level (the so-called "dry dams" which have empty reservoirs prior to flash floods) and relatively slowly recedes. Under these type of hydrological drivers, the stability of the dam's soil requires a special examination [65]. The whole porous body of the dam, rather than a soil column, should be tested under rising-receding hydraulic gradients and pore pressures. In this Section, we extend the analysis from Section 4, i.e., we compare an analytical solution with HYDRUS simulations for a single-maximum hydrograph and a two-layered flow domain.

5.1 Kalashnikov's analytical solution

We consider a vertical cross-section, a rectangle A$_1$E$_1$F$_1$D$_1$ (Fig. 9a) made of a homogeneous material with the hydraulic conductivity k and porosity 휀$_s$. However, unlike as in Section 4, a porous rectangle A$_1$E$_1$F$_1$D$_1$ is underlain by a layer A$_1$D$_1$D$_L$A$_L$, a low-permeable medium, an "aquitard" of the conductivity $k_1 \ll k$ (Figs. 2a and 9a). The thickness f of this layer is small, and the pressure head p along A$_L$D$_L$ is zero. In the analytical solution, we introduce a Cartesian coordinate system xy with the origin A$_1$. Both porous rectangles (Fig. 9a) are initially (t<0) dry. After t=0, the left face of the domain, A$_1$E$_1$, is assigned the pressure head boundary condition corresponding to the reservoir level $h_p(t)$, varying as a one-maximum function shown in Fig. 8. A saturation "tongue" propagates into A$_1$E$_1$F$_1$D$_1$. In terms of the DF model, the thickness $h_B(t,x)$ of the "tongue" A$_1$UW$_B$ (Fig. 9a) obeys the following BVP to the Boussinesq equation:

Fig. 9 The Kalashnikov's straight-line phreatic surface evolving in a vertical cross-section of a two-layered soil displayed together with the HYDRUS FE mesh and boundary conditions (**a**), the HYDRUS-computed isobars at t=40 (**b**) and t=140 min (**c**), and the HYDRUS-computed isotachs at t=100 min (**d**)

a

No-flow boundaries

350 cm

E_1 F_1

VGM sand, k =0.495 cm/min

250 cm

$h_p(t)$

Pressure head varies with time as Kalashnikov's hydrograph

Phreatic surface at the peak of reservoir's hydrograph

Phreatic surface at hydrograph's recession stage

U

h_B

A_1 W_B D_1 x

A_L D_L

f=5cm

Phreatic surface at hydrograph's rising stage

van Genuchten's loamy aquitard, k=0.01733 cm/min

Constant pressure head boundary, p=0

b

U

W_B

-10.000   -8.000   -6.000   -4.000   -2.000   0.000   2.000   4.000   6.000   8.000   10.000

c

d

0.000   0.054   0.109   0.163   0.217   0.271   0.326   0.380   0.434   0.488   0.543   0.597

Velocity - v[cm/min], Min=0.000, Max=0.597

$$\theta_s \frac{\partial h_B}{\partial t} = \frac{\partial}{\partial x}\left(kh_B\frac{\partial h_B}{\partial x}\right) - k_1\frac{h_B}{f}, \qquad q(t,x) = -kh_B\frac{\partial h_B}{\partial x}, \quad 0 < x < x_{WB}(t)$$
$$h_B(t,0) = h_p(t), \quad h_B(0,x) = 0$$

$$(25)$$

where q is the seepage flow rate through a vertical cross-section x and $x_{wB}(t)$ is the locus of the wetting front, point W_B, where $q=0$. Flow is quasi-horizontal and quantified by the first term on the RHS of eq. (25) and indicated by a yellow arrow in Fig. 9a. Leakage through the aquitard is quasi-vertical and described by the second term on the RHS of eq. (25). The corresponding leakage flow rate $q_l(t,x)$ is indicated by a red arrow in Fig. 9a. Equation (25) ignores capillarity and hysteresis: at any point x and at any time t as the phreatic surface h_B rises or drops, the pore water immediately fills or abandons the corresponding interstitial space.

Kalashnikov [58] reported a simple (and well-forgotten by geotechnical engineers) explicit analytical solution to the nonlinear degenerate parabolic PDE (25) for a special one-peak hydrograph:

$$h_p(\tau) = 4h_{p\max}\exp[-\tau](1-\exp[-\tau]) \qquad (26)$$

where h_{pmax} is the maximum of the reservoir level and $\tau = tk/\theta_s$ is a dimensionless time. Kacimov [62] used this solution for assessing a potential impact of the reservoir on a subsurface structure (e.g., a waste repository or a missile silo). Now, we revisit Kalashnikov's solution to compare it with the HYDRUS simulations.

We introduce the following dimensionless variables: $h_{Bd} = h_B/h_{p\max}$, $x_d = x/h_{p\max}$, $f_d = f/h_{p\max}$, $t_d = tk/(\theta_s h_{p\max})$, and $k_r = k_1/k$, and drop the subscript "d". The solution to the problem (25)-(26) is a phreatic surface:

$$h_B(t,x) = 4\exp[-tk_r/f](1-\exp[-tk_r/f]) - 2\exp[-tk_r/f]\sqrt{k_r/f}x,$$
$$0 < x < x_{WB} = 2\exp[-tk_r/f]\sqrt{f/k_r}, \ 0 < t < \infty$$

$$(27)$$

i.e., a segment of a straight line. The slope of this line is always negative, i.e., pore water in the dam is devoured by leakage. There is no seepage back to the reservoir and therefore no threat of suffusion along A_1U (Fig. 9a). Obviously, the aquitard zone adjacent to the A_1A_L line, where the vertical hydraulic gradient varies according to $h_B(t,0)/f$, is most susceptible to translocation of fine particulates from the porous medium of the dam body into the "aquitard."

From Eq. (27), the peak of the hydrograph $h_{pmax}=1$ is attained at $t=f/k_r*\log(2)$; the maximum instantaneous flow rate of seepage from the reservoir into the dam $q_{\max}(t,0) = 32/27\sqrt{k_r/f}$ is attained at $t=f/k_r*\log(3/2)$; the maximum volume of pore water stored in the dam $V_{max}(t) = \max[\theta_s h(t,0)x_{wB}(t)/2] = 16\theta_s/27*\sqrt{f/k_r}$ is attained at $t=f/k_r*\log(3)$; the maximum

propagation width of the wetting front into the dam $x_{WBmax} = 2\sqrt{f/k_r}$ is asymptotically attained at $t=\infty$.

5.2 HYDRUS 2D simulations

For comparisons with the analytical solution (27), the transport domain simulated by HYDRUS is a large sand-made rectangle $A_1E_1F_1D_L$ ($0<X_H<350$ cm, $0<Z_H<250$ cm; the dam body) and the origin of the spatial coordinates is point A_L (Fig. 9a). The thin rectangle $A_1D_1D_LA_L$ (an "aquitard" consisting of a VGM loam) is 5 cm thick. Hysteresis in the soil-water retention function is neglected in both rectangles. Simulations were carried out for 500 min. A time-variable pressure head boundary condition (26) with $h_{pmax}=100$ cm is approximated using a linear interpolation between points at each 10 min (i.e., we used 50 linear interpolation lines to approximate the hydrograph in Fig. 8). Parameters of the FE discretization are as follows: 40x40 layers, 1,681 nodes, 160 1-D elements, and 3,200 2-D elements (Fig. 9a). Figs. 9bc show the isobars around the phreatic surface $p=0$ at $t=40$ min and $t=140$ min, respectively (the hydrograph peak is at $t=89$ min). The colored map of isotachs is shown in Fig. 9d at $t=100$ min. Up to about $t=200$ min, the HYDRUS phreatic surface and the Kalashnikov solution (27) match well. After that, capillarity of the soil in the rectangles prevails, and the numerical and analytical solutions diverge.

6 3-D saturated-unsaturated flow simulated by HYDRUS

In this Section, we consider a 3-D transient saturated-unsaturated flow in a rectangular loam-made parallelepiped of sizes $a*b*c$ (Fig. 2a), where $a=50$ m, $b=200$ m, $c=110$ m, and $d=15$ m. The real dams (see, for example, Fig. 1-49 for the Oroville Dam in [66]) are zoned, with a core, sloping shoulders, drains, and other elements, which have spatially varying and contrasting soil properties. The initial conditions for total pressure heads and/or water contents, which reflect transient conditions of infiltration (determined by rainfall) and reservoir stage variations, may be rather complex. Therefore, a homogeneous flow domain (Fig. 2a) and simple initial and boundary conditions adopted in our HYDRUS-3D [56] simulations given below serve as a simple qualitative analysis and as an asymptotic (at large t) comparison with the analytical solution described in Section 3.

We count the total head from the dam base $y=0$. We assume the following initial conditions: at $t=0$ the total head $h=H_0=2$ m in the parallelepiped $0<x_1<a$, $0<x_2<b$, $0<y<H_0$ (hydrostatic conditions, i.e., no seepage at $t<0$). Above this "thin" parallelepiped, which is at an initial "background"

full saturation, the dam's loam is at negative hydrostatic pressure heads.

We assume the following boundary conditions (see Fig. 2a):

1. The rectangles $A_1E_1F_1D_1$ (the plane of symmetry, the front face of the flow domain), $A_1A_2D_3D_1$ (the dam base), $A_2B_3F_3D_3$ (the back face of the flow domain) and $D_1F_1F_2D_2$ (the vertical barrier, a shaded area in Fig. 2a) are no-flow boundaries.
2. The rectangle $D_2C_2C_3D_3$ (the lower right face of the flow domain) remains at a constant total head $h=H_0 = 2$ m (a static tailwater level) at all times.
3. The rectangle $C_2F_2F_3C_3$ (the upper right face of the flow domain) is a potential seepage face, which transmits water to the atmosphere from the 3-D flow domain (an actual seepage face) when the pore pressure on its outflow side becomes positive and is impermeable otherwise.
4. The "expanding" rectangle $A_1A_2B_3B_1$ (the lower left face of the flow domain) is the surface of a contact between the rising and (eventually) static reservoir water level. We assume that the total head initially varies linearly:

$$h = H_0 + R^*t \text{ at } 0 < t < T_{rise} \qquad (28)$$

where $R^*=1$ m/day is the rate of the reservoir water level rise and $T_{rise}=100$ days is the duration of the rise. At $t>T_{rise}$, the water level in the reservoir remains constant and therefore the boundary condition along a stabilized rectangle $A_1A_2 B_3B_1$ is $h=102$ m at $t>100$ days.

5. The rectangle $B_1E_1E_2B_3$ (the middle left face of the flow domain), which "shrinks" at $0<t<T_{rise}$ is impermeable.
6. The rectangle $E_1E_2F_3F_1$ (the upper face of the flow domain) is a no-flow zone.

HYDRUS [56] simulates saturated-unsaturated flow governed by Richards' equation in the 3-D transport domain, which is discretized into finite elements of triangular prisms. We used default HYDRUS parameters, such as iteration criteria, time-step controls, the VGM soil hydraulic functions, the built-in Soil Catalogue [67], etc.

We selected the "3-D simple" domain type with the following dimensions: 50x200x110 m in the X_H, Y_H, and Z_H Cartesian coordinates of HYDRUS (Fig. 10a), with the origin at point A_1 (see also Fig. 2a where the corresponding coordinates were x_1, x_2, and y). Triangular prisms were selected for the FE discretization of the parallelepiped with 41, 27, and 87 layers in the X_H, Y_H, and Z_H directions, respectively. The total number of nodes was 96,309, and the finite element mesh involved 132, 2,080, and 178,880 1-D, 2-D, and 3-D elements, respectively. Seven observation points were placed at characteristic locations of the parallelepiped for monitoring the dynamics of flow parameters.

We assumed the following initial ($t=0$ d) conditions: the total head (counted from the $Z_H=0$ plane in Fig. 10a) was $H_0=2$ m in the entire transport domain ($0<X_H<50$ m, $0<Y_H<200$ m, $0<Z_H<110$ m) (i.e., hydrostatic conditions, with no seepage at $t<0$). The transport domain is thus initially fully saturated for $Z_H<2$ m and has negative hydrostatic pressure heads for $Z_H>2$ m. The simulation was carried out for $0<t<365$ days. We recall that the boundary condition along the reservoir face $X_H=0$ was time variable. A snapshot of $t=365$ days was selected for visualization of the results.

We assumed that the dam is made of a homogeneous, isotropic, incompressible loam with the following van Genuchten soil hydraulic parameters selected from the HYDRUS Soil Catalogue: the saturated hydraulic conductivity $k_1=0.25$ m/day, porosity of 0.43, the irreducible volumetric water content of 0.078, and the van Genuchten parameters of the soil water retention curve 훼 = 3.6 1/m and $n=1.56$. We assumed no rainfall on the ground surface $Z_H=110$ m and no root water uptake from the dam soil.

Simulations corroborate our concerns about the seepage-induced threat to the dam's stability. For example, Fig. 10g shows that along the major area of the seepage face the magnitude of the hydraulic gradient exceeds 1. Moreover, close to the edge of the barrier (the vertical line $X_H=50$ m, $Y_H=15$ m) extremely high gradients (exceeding 10) are apparent, similarly as obtained by the analytical solution given in Fig. 4b.

7 Concluding remarks

Factors around (actual and potential) failure of dams' spillways can be assessed with both analytic and numerical tools, and the paper presented what we learn from that analysis. Our objective was to use computer algebra and a FEM model to study the fields of the hydraulic gradients (or Darcian velocities), total hydraulic heads, and pore pressures within a porous dam body, in particular, in the locus of static and transient phreatic surfaces. We developed new analytical solutions, revisited the old ones, and surveyed the methods as they pertain to the problems of seepage in earth dams. We used and cross-compared the results of computations in:

- analytical models for quasi 3-D steady DF flow, potential transient 2-D phreatic surface seepage governed by Laplace's equation in a dam body resting on an impermeable substratum;
- an analytical model for 1-D Boussinesq flow over a leaky bottom;
- a numerical FEM model for saturated-unsaturated flows governed by Richards' equation.
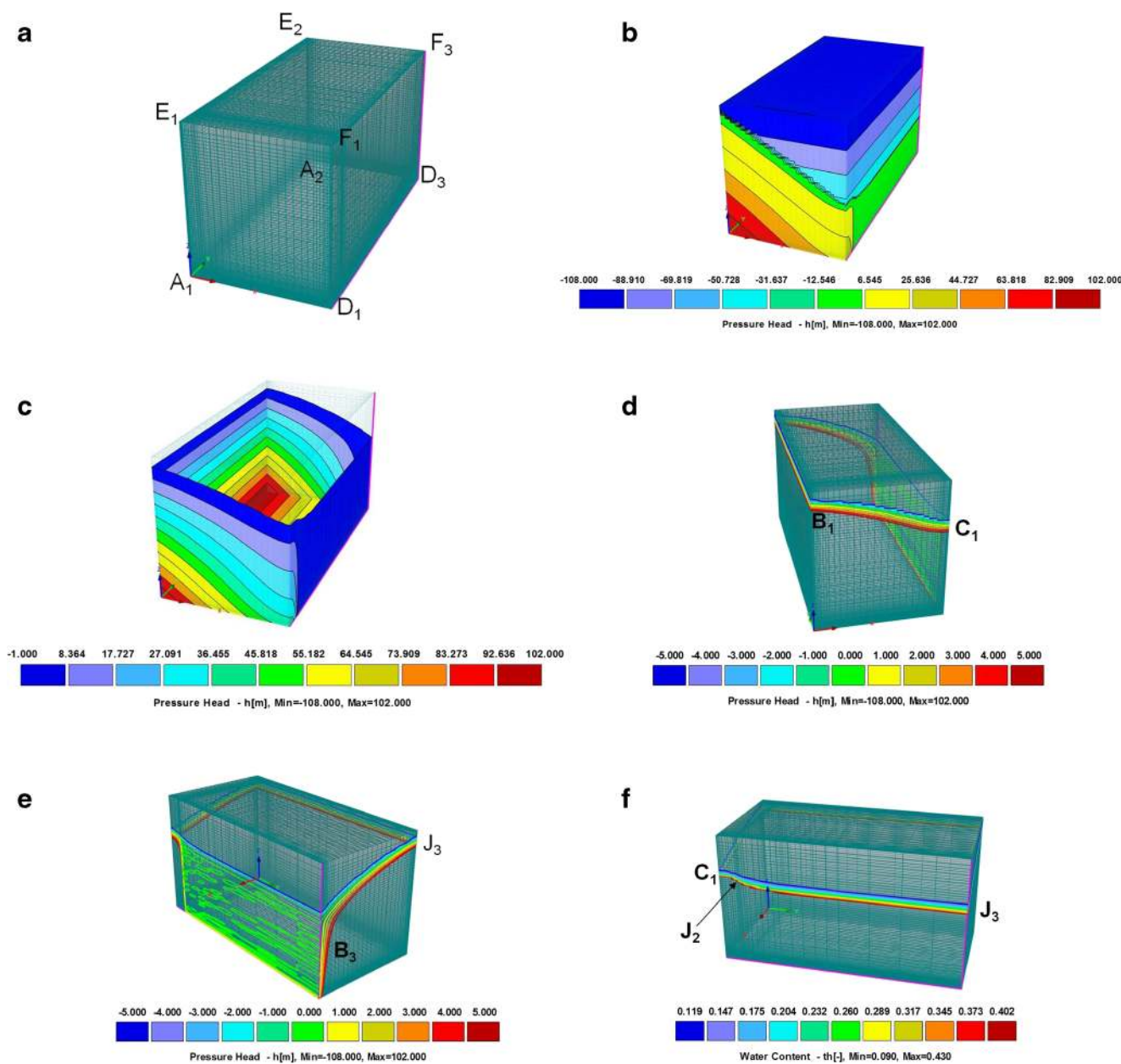
Fig. 10 The 3-D HYDRUS transport domain with finite element discretization (**a**), the distribution of the pressure head p at t=100 d (**b**), the positive pressure heads at t=365 d at the shell of the transport domain (**c**), isobaric contours around the phreatic surface displayed on the shell of the transport domain at the left (Y_H=0) and back (X_H=0) planes (**d**) and right (Y_H=200 m) and front (X_H=50 m) planes (**e**), contours of volumetric water contents in the capillary fringe above the phreatic surface at the front plane (X_H=50 m) at t=365 d (**f**), isotachs at the front plane (X_H=50 m) at t=365 d (**g**), and isobars, isotachs, and velocity vectors in the cross-sectional plane (Z_H=2 m) at t=365 d (**h**)

The numerical and analytical solutions presented in our paper, generally speaking, match well. They indicate that under selected initial and boundary conditions, the dam soil adjacent to an impermeable barrier is indeed under a high risk of erosion due to seepage. As parametric inputs to our models, we assumed simple flow geometries (rectangles and box-shaped domains) and soil homogeneity with respect to the saturated hydraulic conductivity and VGM capillary constants. The real dam body went through a decade-long consolidation-differential settlement that in terms of our models would have resulted in the heterogeneity of k, θ_s, θ_r, and VGM parameters, the anisotropy of k, and perhaps, hysteresis (not only in water retention curves but perhaps also in relative permeability functions). Consequently, more realistic geometries (for example, a truncated prism as the dam body, i.e., a trapezium rather than a rectangle in a vertical cross-section) and heterogeneity of soil (rock) filling can be modeled in the future by HYDRUS. For this extended modeling, as well as for validation of both analytical
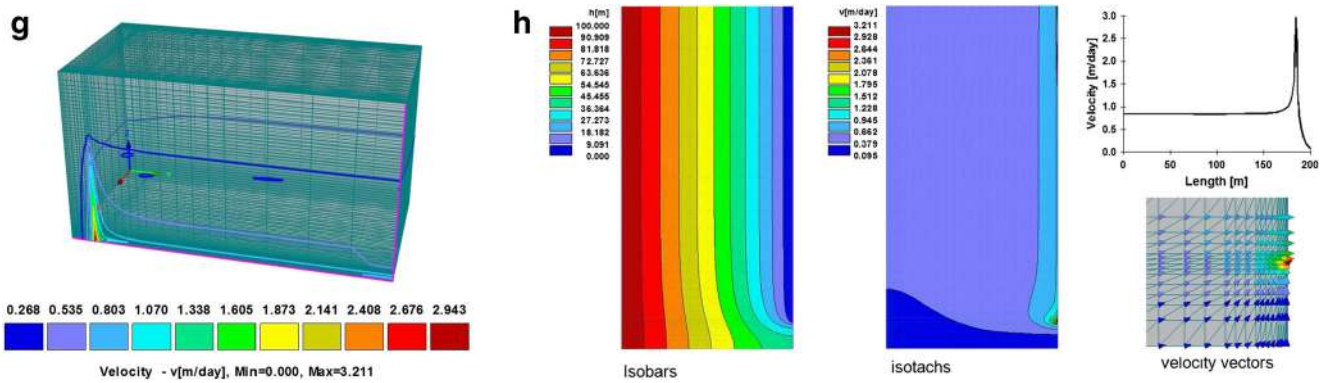
Fig. 10 (continued)

and numerical solutions (and for falsification of Hegel's skepticism about historical lessons), in the application to the particular case of the Oroville Dam, the following information would be beneficial:

- systematic (regular) historic records from piezometers/ moisture content data loggers with interpolated dynamic fields of 3-D transient pressure heads in the interior of the dam;
- several infiltration tests on the dam slopes and crest for the assessment of hydraulic properties of the soil surface and, consequently, the prediction of accretion to the phreatic surface during rainfall events and of evapotranspiration during dry spells;
- several geophysical surveys (e.g., by OhmMapper, gravi-meters, sap flow meters used for the plants emerging on the downstream slope of the dam) with transects parallel and perpendicular to the dam crest for proxy-data on the moisture content/pore pressure distributions, plant roots' topology, and position of the phreatic surface in the dam body, the following phenomena.

The modeling-data acquisition/processing program for the Oroville dam can serve as a prototype for many other monitoring-maintenance programs applied to hydraulic infra-structure in the USA, and many other countries.

Abbreviations BVP, boundary value problem; DF, Dupuit-Forchheimer; PDE, partial differential equation; PK-77, reference to the book [57]; RHS, right hand side; VGM, van Genuchten – Mualem model

References

1. Strack, O.D.L.: Groundwater mechanics. Prentice-Hall, Inc., Englewood Cliffs (1989)

2. Yakimov, N.D., Kacimov, A.R.: Darcian flow under/through a leaky cutoff-wall: Terzaghi-Anderson's seepage problem revisited. Int. J. Numer. Anal. Methods Geomech. **41**, 1182–1195 (2017). https://doi.org/10.1002/nag.2668

3. France, J.W., Alvi, I.A., Dickson, P.A., Falvey, H.T., Rigbey, S.J. and Trojanowksi, J.: Independent forensic teamreport: oroville dam spillway incident. url: https://damsafety.org/sites/default/files/files/ IndependentForensicTeamReportFinal01–05-18.pdf 2018 Accessed September 7, 2019

4. Koskinas, A., Tegos, A., Tsira, P., Dimitriadis, P., Iliopoulou, T., Papanicolaou, P., Koutsoyiannis, D., Williamson, T.: Insights into the Oroville dam 2017 spillway incident. Geosciences. **9**(1), 37 (2019). https://doi.org/10.3390/geosciences9010037 Accessed September 7, 2019

5. Bea, R. G., 2017a. Preliminary root causes analysis of failures of the Oroville dam gated spillway. Center for Catastrophic Risk Management, University of California Berkeley, April 17, 2017

6. Bea, R.G.: Legislative oversight testimony report: Oroville dam. Center for Catastrophic Risk Management, University of California Berkeley, May. **11**, 2017 (2017b)

7. Vahedifard, F., AghaKouchak, A., Ragno, E., Shahrokhabadi, S., Mallakpour, I.: Lessons fromthe Oroville dam. Science. **355**(6330), 1139–1140 (2017)

8. Bea, R., Cobos-Roa, D., Storesund, R.: Discussion of "overview of New Orleans levee failures: lessons learned and their impact on national levee design and assessment" by GL Sills, ND Vroman, RE Wahl, and NT Schwanz. J. Geotech. Geoenviron. Eng. ASCE. **135**(12), 1991–1994 (2009)

9. Cobos-Roa, D., Bea, R.: Three-dimensional seepage effects at three New Orleans levee breaches during Hurricane Katrina. Electron. J. Geotech. Eng. **13**, 1–26 (2008)

10. Steedman, R.S., Sharp, M.K.: Physical modelling analysis of the New Orleans levee breaches. Proc. Inst. Civil Eng. Geotech. Eng. **164**(6), 353–372 (2011)

11. National Research Council: Dam and levee safety and community resilience: a vision for future practice. National Academies Press (2012)

12. Chang, D.S., Zhang, L.M.: Extended internal stability criteria for soils under seepage. Soils Found. **53**(4), 569–583 (2013)

13. Zhang, L.M., Chen, Q.: Seepage failure mechanism of the Gouhou rockfill dam during reservoir water infiltration. Soils Found. **46**(5), 557–568 (2006)

14. Vahedifard, F., Robinson, J.D., AghaKouchak, A.: Can protracted drought undermine the structural integrity of California's earthen levees? J. Geotech. Geoenviron. Eng. ASCE. **142**(6), 02516001 (2016)

15. Vano, J.A., Miller, K., Dettinger, M.D., Cifelli, R., Curtis, D., Dufour, A., Olsen, J.R., Wilson, A.M.: Hydroclimatic extremes as

challenges for the water management community: lessons from Oroville dam and hurricane Harvey. Bull. Am. Meteorol. Soc. **100**(1), S9–S14 (2019)

16. Bonelli, S. (ed.): Erosion in geomechanics applied to dams and levees, p. 17. Wiley, London (2013)

17. Istomina, V. S.: Soil stability against seepage. Gosstrojizdat, Moscow (in Russian) (1957)

18. Zhilenkov, V.N.: Hydroisolation properties of soils making cores and liners in large Dams. Energiya, Leningrad (in Russian). (1968)

19. Bendahmane, F., Marot, D., Alexis, A.: Experimental parametric study of suffusion and backward erosion. J. Geotech. Geoenviron. Eng. ASCE. **134**(1), 57–67 (2008)

20. Ke, L., Takahashi, A.: Strength reduction of cohesionless soil due to internal erosion induced by one-dimensional upward seepage flow. Soils Found. **52**(4), 698–711 (2012)

21. Rönnqvist, H., Viklander, P.: Effects of suffusion in embankment dam filters. Dams Reservoirs. **26**(3), 118–125 (2016)

22. Sail, Y., Marot, D., Sibille, L., Alexis, A.: Suffusion tests on cohesionless granular matter: experimental study. Eur. J. Environ. Civ. Eng. **15**(5), 799–817 (2011)

23. Skempton, A.W., Brogan, J.M.: Experiments on piping in sandy gravels. Géotechnique. **44**(3), 440–460 (1994)

24. Crank, J.: Free and moving boundary problems. Clarendon Press, Oxford (1984)

25. Design of Small Dams: USBR-ISDI. Washington (1987)

26. Engemoen, W.: Methods to mitigate internal erosion risks in existing embankment dams. Proc. "6th International Conference on Scour and Erosion", pp. 1567–1575. Paris (2012)

27. Fell, R., MacGregor, P., Stapledon, D., Bell, G.: Geotechnical Engineering of Dams. Balkema, Leiden (2005)

28. FEMA (Federal Emergency Management Agency): Filters for embankment dams – best practices for design and construction. (2011)

29. Hansen, D., Roshanfekr, A.: Assessment of potential for seepage induced unraveling failure of flow-through rockfill dams. Int. J. Geomech. ASCE. **12**(5), 560–573 (2012)

30. ICOLD: Internal erosion of existing dams, levees and dikes, and their foundations. Bulletin. Volume 1: Internal Erosion Processes and Engineering Assessment. ICOLD, Paris (2013)

31. Moran, R., Toledo, M.A.: Research into protection of rockfill dams from overtopping using rockfill downstream toes. Can J. Civ. Eng. **38**, 1314–1326 (2011)

32. Nichiporovich, A.A.: Dams of Local Materials. Strojizdat, Moscow (1973) (in Russian)

33. Peter, P.: Canal and River Levees. Elsevier, Amsterdam (1982)

34. Wan, C.F., Fell, R.: Assessing the potential of internal erosion and suffusion in embankment dams and their foundations. J. Geotech. Geoenviron. Eng. ASCE. **134**(3), 410–407 (2008)

35. Wolff, T.F.: Performance of levee under seepage controls: A critical review (No. ERDC/GSL-TR-02-19). Vicksburg Lab (2002)

36. Troyanowski, J.: Dam safety: Evaluating spillway condition. http://www.hydroworld.com/articles/hr/print/volume-27/issue-2/technical-articles/dam-safety-evaluating-spillway-condition.html (2008) Accessed September 7, 2019

37. Casagrande, A.: Seepage through dams. J. N. Engl. Water Works. **51**, 295–336 (1937)

38. Cedergren, H.R.: Seepage, drainage and flow nets. Wiley, New York (1989)

39. Rochim, A.,Marot, D., Sibille, L., Thao Le, V.: Effects of hydraulic loading history on suffusion susceptibility of cohesionless soils. J. Geotech. Geoenviron. Eng. ASCE. 143(7), paper 04017025 (2017)

40. van Genuchten, M.T.: A closed-form equation for predicting the hydraulic conductivity of unsaturated soils. Soil Sci. Soc. Am. J. **44**, 892–898 (1980)

41. Chapius, R.P., Aubertin, M.: A simplified method to estimate saturated and unsaturated seepage through dikes under steady- state conditions. Can. Geotech. J. **38**, 1321–1328 (2002)

42. Desai, C.S.: Seepage analysis of earth banks under drawdown. J. SoilMech. Found. Eng. Div. ASCE. **98**(SM11), 1143–1162 (1972)

43. Federico, F., Calzoletti, F., Montanaro, A.: Steady state seepage flow through zoned earth structures affected by permeability defects. In: Numerical Methods in Geotechnical Engineering, pp. 311–316. Taylor & Francis, London (2010)

44. Freeze, R.A.: Influence of the unsaturated flow domain on seepage through earth dams. Water Resour. Res. **7**(4), 929–941 (1971)

45. Ilyinsky, N.B., Kacimov, A.R., Yakimov, N.D.: Designing the shape of soil slopes stable during seepage in Californian hillsides. In: Chandler, R.J. (ed.) Slope stability engineering. proc. of the international conf. on slope stability, pp. 67–70. Thomas Telford, London (1991)

46. Ilyinsky, N.B., Kacimov, A.R., Yakimov, N.D.: Analytical solutions of seepage theory problems. Inverse methods, variational theorems, optimization and estimates (A review). Fluid Dyn. **33**(2), 157–168 (1998)

47. Kacimov, A.R., Obnosov, Y.V.: Analytical solutions for seepage near material boundaries in dam cores: the Davison-Kalinin problems revisited. Appl. Math. Model. **36**, 1286–1301 (2012). https://doi.org/10.1016/j.apm.2011.07.088

48. Lee, S.S., Yamashita, T.: Finite-difference method three dimensional model for seepage analysis through Fordyce dam. In Advances in Geosciences. Hydrological Science. **6**, 171–180 (2007)

49. Liggett, J.A., Liu, P.L.-F.: Unsteady interzonal free surface flow in porous media. Water Resour. Res. **15**(2), 240–246 (1979)

50. Neuman, S.P., Witherspoon, P.A.: Finite element method of analyzing steady seepage with a free surface. Water Resour. Res. **6**(3), 889–897 (1970)

51. Rehbinder, G.: Relaxation of pore pressure in a slender core of a rockfill dam. J. Hydraul. Res. **35**(2), 161–176 (1997)

52. Stark, T.D., Jafari, N.H., Zhindon, J.S.L., Baghdady, A.: Unsaturated and transient seepage analysis of San Luis dam, p. 04016093. J. Geotech. Geoenviron. Eng. ASCE (2016)

53. Vandenboer, K., van Beek, V., Bezuijen, A.: 3D finite element method (FEM) simulation of groundwater flow during backward erosion piping. Front. Struct. Civ. Eng. **8**(2), 160–166 (2014)

54. Alvi, I. A., 2013. Engineers need to get real, but can't: The role of models. In Structures Congress 2013: Bridging Your Passion with Your Profession, 916–927

55. Kacimov, A.R., Yakimov, N.D.: Moving phreatic surface in a porous slab: an analytical solution. J. Eng. Math. **40**, 399–411 (2001)

56. Šimůnek, J., van Genuchten, M.T., Šejna, M.: Recent developments and applications of the HYDRUS computer software packages. Vadose. Zone. J. **15**(7), (2016). https://doi.org/10.2136/vzj2016.04.0033

57. Polubarinova-Kochina PY (1962, 1977) Theory of ground water movement. Princeton University Press, Princeton. Second edition of the book in Russian is published in 1977, Nauka, Moscow

58. Kalashnikov, A.S.: Some problems of the qualitative theory of non-linear degenerate second-order parabolic equations. Russ. Math. Surv. **42**, 135–176 (1987)

59. Haitjema, H.M.: Analytic element modelling of groundwater flow. Academic Press, San Diego (1995)

60. Wolfram, S.: Mathematica. A system for doing mathematics by computer, Addison-Wesley, Redwood City (1991)

61. Blunt, M.J.: Multiphase flow in permeable media: a pore-scale perspective. Cambridge University Press, Cambridge (2017)

62. Kacimov, A.R.: Estimation and optimization of transient seepage with free surface. J. Irrigation and Drainage Engrg. **119**(6), 1014–1025 (1993)

63. Kacimov, A., Obnosov, Y. V. and Or, D.: Evaporation induced capillary siphoning through hydraulically connected porous domains: the Vedernikov-Bouwer model revisited. Transp Porous Med (Springer) in press (2019) 129: 231. https://doi.org/10.1007/s11242-019-01285-z

64. Kacimov, A.R., Brown, G.: A transient phreatic surface mound, evidenced by a strip of vegetation in an earth dam shoulder. Hydrol. Sci. J. **60**(2), 361–378 (2015)

65. Jia, G.W., Zhan, T.L.T., Chen, Y.M., Fredlund, D.G.: Performance of a large-scale slope model subjected to rising and lowering water levels. Eng. Geol. **106**(1–2), 92–103 (2009)

66. Jansen, R. B.: Dams and public safety. Available from U. S. Government Printing Office, Washington D. C. 20402 Stock, (024–003). (1980)

67. Carsel, R.F., Parrish, R.S.: Developing joint probability distributions of soil water retention characteristics. Water Resour. Res. **24**, 755–769 (1988)

68. USACoE: National Inventory of Dams. http://nid.usace.army.mil/cm_apex/f?p=838:1:0::NO (2016)